Increased Variability of Biomass Burning Emissions in CMIP6 Amplifies Hydrologic Cycle in the CESM2 Large Ensemble

Kyle Benjamin Heyblom[1], Hansi Alice Singh[1], Philip J. Rasch[2], and Patricia DeRepentigny[3]

[1]University of Victoria
[2]Pacific Northwest National Laboratory (DOE)
[3]University of Colorado Boulder

November 24, 2022

Abstract

Historical simulations performed for the Coupled Model Intercomparison Project Phase 6 (CMIP6) used biomass burning emissions between 1997–2014 containing higher spatial and temporal variability compared to emission inventories specified for earlier years, and compared to emissions used in previous (e.g., CMIP5) simulation intercomparisons. Using the Community Earth System Model version 2 (CESM2) Large Ensemble, we show this increased biomass burning emissions variability leads to amplification of the hydrologic cycle poleward of 40°N. Notably, the high variability of biomass burning emissions leads to increased latent heat fluxes, column-integrated precipitable water, and precipitation. Lower relative humidity, greater static stability, greater ocean heat uptake, and weaker meridional energy transport from the tropics act to moderate this hydrologic cycle amplification. Our results suggest it is not only the secular changes (on multidecadal timescales) in biomass burning emissions that impact the hydrologic cycle, but also the shorter timescale variability of their emissions.

Increased Variability of Biomass Burning Emissions in CMIP6 Amplifies Hydrologic Cycle in the CESM2 Large Ensemble

Kyle B. Heyblom[1], Hansi A. Singh[1], Philip J. Rasch[2,3], Patricia DeRepentigny[4]

[1]University of Victoria, School of Earth and Ocean Sciences, Victoria, BC, Canada
[2]Pacific Northwest National Laboratory, Atmospheric Sciences and Global Change Division, U.S. DOE Office of Science, Richland, WA, USA
[3]University of Washington, Department of Atmospheric Science, Seattle, WA, USA
[4]National Center for Atmospheric Research, Climate and Global Dynamics Laboratory, Boulder, CO, USA

Key Points:

- Increased biomass burning emissions variability in CMIP6 amplifies hydrologic cycle in CESM2
- Column-integrated precipitable water, evaporation, and precipitation all increase poleward of 40°N
- Several moderating factors act to mitigate hydrologic cycle amplification

Corresponding author: Kyle B. Heyblom, `kheyblom@uvic.ca`

Abstract

Historical simulations performed for the Coupled Model Intercomparison Project Phase 6 (CMIP6) used biomass burning emissions between 1997–2014 containing higher spatial and temporal variability compared to emission inventories specified for earlier years, and compared to emissions used in previous (e.g., CMIP5) simulation intercomparisons. Using the Community Earth System Model version 2 (CESM2) Large Ensemble, we show this increased biomass burning emissions variability leads to amplification of the hydrologic cycle poleward of 40°N. Notably, the high variability of biomass burning emissions leads to increased latent heat fluxes, column-integrated precipitable water, and precipitation. Lower relative humidity, greater static stability, greater ocean heat uptake, and weaker meridional energy transport from the tropics act to moderate this hydrologic cycle amplification. Our results suggest it is not only the secular changes (on multidecadal timescales) in biomass burning emissions that impact the hydrologic cycle, but also the shorter timescale variability of their emissions.

Plain Language Summary

Global climate models use different inputs to simulate the past climate as accurately as possible. One of these inputs is an estimate of emissions from the burning of biomass (e.g., from forests and cropland). In the sixth phase of the Climate Model Intercomparison Project (CMIP6), the estimated biomass burning emissions were derived using two very different methods. Prior to 1997, emission estimates relied on a combination of indirect measurements and best-guess fire modelling resulting in emissions having relatively modest temporal and spatial variability. During later periods (i.e., 1997–2014) satellite based estimates of fire occurrence and intensity were used in combination with biogeochemical models to produce emission estimates containing much larger spatial and temporal variability. This study demonstrates that the differing variability in biomass burning has an impact on the model's water cycle. During years of strong burning episodes, clouds thin and more sunlight reaches the surface, which results in more surface evaporation, and higher atmospheric humidity, and precipitation. Additionally, the high variation in emissions increases rainfall, decreases snowfall, and increases the intensity of extreme precipitation events. Our results show that the timing of biomass burning emissions, not just the amount emitted, is an important moderator of the atmospheric water cycle.

1 Introduction

Many factors affect the atmospheric hydrologic cycle, and aerosols are among the most important of these factors. Aerosols impact regional and global scale precipitation through their direct radiative forcing and indirect microphysical effects (e.g., see Boucher et al., 2013; Ramanathan et al., 2001, and references therein). Simulation of the hydrologic cycle in historical and future projections is highly dependent on accurate modelling of aerosols. Indeed, aerosol-cloud interactions and their associated radiative forcing are among the most uncertain components of the historical radiative forcing of Earth's climate (Boucher et al., 2013; Flato et al., 2013; Kiehl, 2007; Seinfeld et al., 2016).

While aerosols are a topic of great interest to the climate community, comparatively little attention has been directed to how the variability of aerosol emissions affect the climate system (rather than the total amount of such emissions). Most current knowledge is based on idealized scenarios. For example, the latest Geoengineering Model Intercomparison Project Phase 6 (GeoMIP6; Kravitz et al., 2015) experiments only prescribe emissions as either constant in time, increasing at a fixed rate, or as an instantaneous change. The Model Intercomparison Project on the climatic response to volcanic forcing (VolMIP; Zanchettin et al., 2016) and the fourth phase of the Paleoclimate Model Intercomparison Project (PMIP4; Jungclaus et al., 2017) do consider the effect of volcanic emissions, which are necessarily episodic. However, the volcanic events simulated in these experiments are large and occur infrequently (i.e., they are years to decades apart). Such studies did not explore the climate impact of interannual emissions variability, or compare the impacts of variable aerosol emissions to continuous emissions.

Unlike the emissions used in many previous intercomparison activities, the biomass burning emissions prescribed for the sixth phase of the Climate Model Intercomparison Project (CMIP6) historical simulations (BB4CMIP6; see van Marle et al., 2017) contain separate periods characterized by low and high interannual variability, thereby providing an opportunity to explore how such variability impacts the climate system. The methods and measurements used to construct this aerosol emission inventory utilized a variety of strategies over different intervals within the historical (1850–2014) period that produce different variability in estimated emissions. Between 1997 and 2014, the Global Fire Emissions Database version 4 with small fires (hereafter GFED; van der Werf et al., 2017) was used to estimate biomass burning emissions. These estimates include much higher temporal variability compared to prior years. Similar strategies were used for other aerosol sources (Hoesly et al., 2018). The interannual variability of black carbon, sulfate, and primary organics emitted between 40-70°N during 1997–2014 is approximately six times greater than the 18 years prior to it (as assessed from the standard deviation; see Figure 1a, black line). This large change in variability is new to the CMIP6 forcing and was not present in CMIP5, where decadal means were used to construct historical gridded biomass burning emissions (Lamarque et al., 2010). The prescribed biomass burning emissions largely consist of primary aerosols and reactive gases (van Marle et al., 2017), many of which result in the formation of secondary organic aerosols (Pandis et al., 1992).

Recent studies by DeRepentigny et al. (2021) and Fasullo et al. (2021) have compared the climate impacts of these (high variability) BB4CMIP6 emissions with simulations using emissions with less variability. Both studies find that it is not only the magnitude of aerosol emissions that impact the climate system, but also their temporal variability. Fasullo et al. (2021) showed that the sudden increase in aerosol emissions variability from 1997–2014 acts to decrease cloud droplet number concentrations and low cloud amount, which increases downwelling shortwave radiation. DeRepentigny et al. (2021) further showed that greater variability in biomass burning emissions accelerated Arctic sea ice loss over this time period. Given that aerosols have a profound impact on the hydrologic cycle, a natural question that arises is the following: how does such a change in the temporal variability of biomass burning emissions affect the hydrologic cycle?

This study addresses this very question. Following the findings of DeRepentigny et al. (2021) and Fasullo et al. (2021), the Community Earth System Model version 2 Large Ensemble Community Project (CESM2-LE; Rodgers et al., 2021) forced half of its ensemble members with the original CMIP6 biomass burning emissions, and the second half with smoothed biomass burning emissions during the period of increased variability (from 1997–2014; Figure 1a, red line). Here, we utilize these two sets of simulations to investigate the impact that this increase in biomass burning emissions variability has on the global atmospheric hydrologic cycle. We find the high variability of biomass burning emissions amplifies all elements of the atmospheric hydrologic cycle, from evaporation to column-integrated precipitable water to precipitation. Conversely, we find that several moderating factors act to mitigate this amplification of the hydrologic cycle. We conclude with a discussion of the implications of our findings for research utilizing CMIP6 output over the historical period.

2 Model Data

We assess the impact of biomass burning emissions variability on the atmospheric hydrologic cycle using the Community Earth System Model version 2 Large Ensemble Community Project (CESM2-LE; Rodgers et al., 2021). This large ensemble project used the fully coupled CESM2 configured with the Community Atmosphere Model version 6 (CAM6; Danabasoglu et al., 2020), Parallel Ocean Program version 2 (POP2; Smith et al., 2010), Los Alamos Sea Ice Model version 5.1.2 (CICE5; Hunke et al., 2015), and Community Land Model version 5 (CLM5; Lawrence et al., 2019). Aerosols were simulated using the four-mode version of the Modal Aerosol Module (MAM4; Liu et al., 2016). Each component was configured at a nominal 1° spatial resolution (Rodgers et al., 2021).

We analyze 80 CESM2-LE ensemble members subject to historical emissions (1850–2014) and the future SSP3-7.0 emissions (a medium-to-high emission scenario from 2015–2100; see O'Neill et al., 2016). Half of these 80 members were forced with the standard CMIP6 biomass burning emissions (hereafter HiVarBB; Figure 1a, black line; van Marle et al., 2017). The other half instead used a temporally smoothed biomass burning emission inventory (hereafter SmoothBB; Figure 1a, red line). This temporal smoothing was achieved by using an 11-year running mean filter from 1990–2020. This smoothing method reduced the interannual variability such that it aligned more closely with the variability of biomass burning emissions before the GFED period (1997–2014), but still nearly preserved the total cumulative amount of aerosol emissions through this period. Because fires varied from one year to another, the temporally smoothed emission inventory is also spatially smoother. The 80 members were initialized from four different years of the pre-industrial control simulation (years 1231, 1251, 1281, and 1301). Each initialization year was selected based on the phase of the Atlantic Meridional Overturning Circulation (AMOC) strength (see Rodgers et al., 2021). Twenty members were started from each initialization year by randomly perturbing the temperature field. Half of each 20 member set used the HiVarBB emissions, while the other half used the SmoothBB emissions. We evaluate the relative impact of the increase in biomass burning variability by comparing the HiVarBB and SmoothBB simulations over the GFED period (1997–2014).

3 Cloud and Surface Radiative Response

In the CESM2-LE, the choice of biomass burning emissions (HiVarBB or SmoothBB; Figure 1a, black and red lines, respectively) impacts clouds and surface radiation. Cloud droplet number (CDN) concentrations are lower in ensemble members subjected to the CMIP6 biomass burning emissions relative to those subjected to the smoothed biomass burning emissions during the GFED period (i.e., the average of HiVarBB ensemble members minus the average of the SmoothBB ensemble members from 1997 to 2014; Figure 1b). The difference in CDN concentrations is particularly large over the North American and Asian boreal regions. This cloud thinning effect in HiVarBB ensemble members, relative to SmoothBB ensemble members, leads to greater surface absorption of shortwave radiation: less shortwave radiation is reflected by clouds, so more reaches the surface (Figure 1c). This larger net surface shortwave radiation leads to surface warming in HiVarBB ensemble members relative to SmoothBB ensemble members during the GFED period (Figure 1d). These findings are in general agreement with similar experiments performed by DeRepentigny et al. (2021) and Fasullo et al. (2021).

4 Hydrologic Cycle Response

We find that the hydrologic cycle strengthens when biomass burning emissions variability is high during the GFED period. Surface latent heat fluxes are greater in HiVarBB ensemble members compared to SmoothBB ensemble members over most of the area poleward of 40°N (Figure 2a). In general, regions with greater latent heat fluxes correspond to those that experience more surface shortwave heating (compare spatial patterns of net surface shortwave flux differences and latent heat flux differences in Figures 1c and 2a, respectively). Poleward of 40°N, the surface latent heat flux is 0.8% (0.3 W/m^2) larger in the HiVarBB ensemble members compared to the SmoothBB ensemble members during the GFED period (Figures 2b, S1a).

These greater latent heat fluxes in the HiVarBB simulations are accompanied by greater column-integrated precipitable water over most of the Northern Hemisphere (NH) relative to the SmoothBB simulations (Figure 2c). Regional differences are statistically significant over most regions of the NH and all regions north of 30°N. Poleward of 40°N, the area-averaged column-integrated precipitable water is 1.4% (0.2 kg/m^2) larger in the HiVarBB simulations

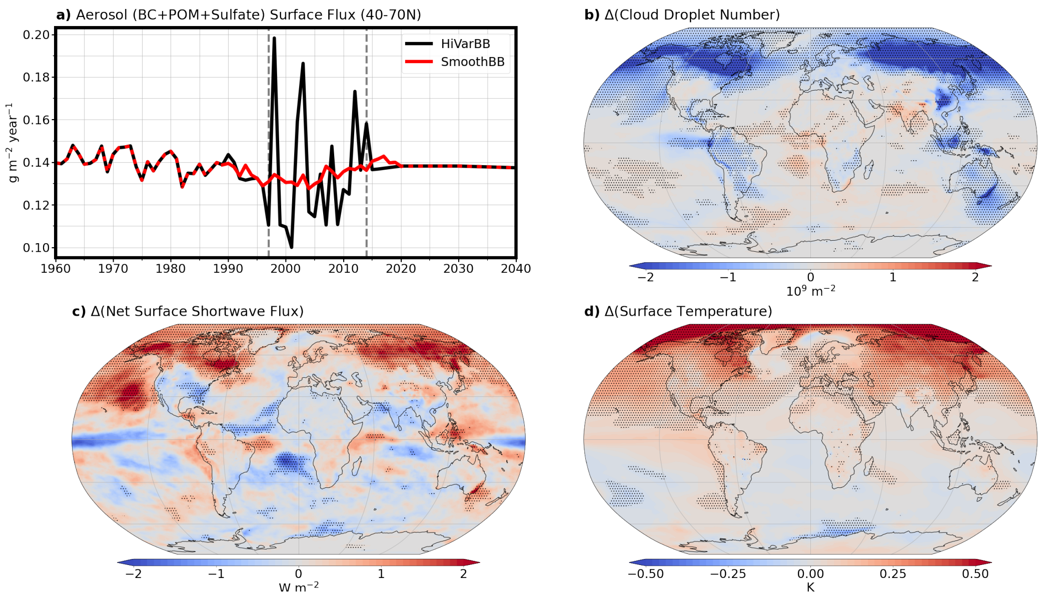

Figure 1. Aerosol emission scenarios and resulting differences in cloud and radiative responses. Panel (a) shows the annual mean sum of black carbon, primary organic, and sulfate aerosol surface fluxes from HiVarBB (black line) and SmoothBB (red line) ensemble sets averaged from 40-70°N, with the vertical gray dashed lines delineating the GFED period (1997–2014). Panels (b-d) show ensemble mean differences (average of HiVarBB ensemble members minus average of SmoothBB ensemble members) in (b) vertically-integrated cloud droplet number concentration, in 10^9 m^{-2}; (c) net surface shortwave flux, in W m^{-2}; and (d) surface temperature, in K, during the GFED period (1997–2014). Stippling signifies 95% confidence in the significance of the difference between ensemble member sets (see Text S1).

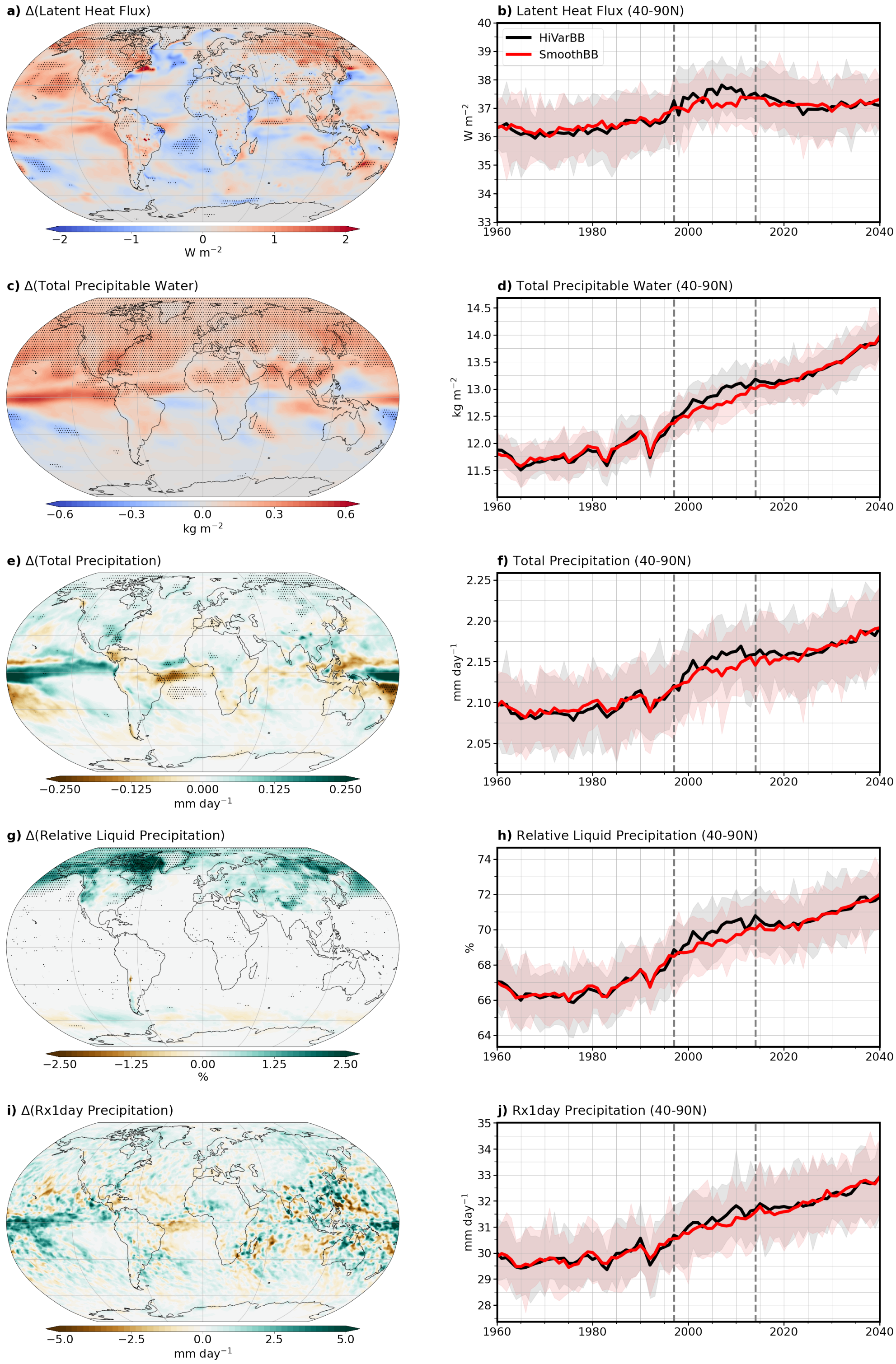

Figure 2. Differences in the atmospheric hydrologic cycle. (a,b) latent heat flux, in W m^{-2}; (c,d) column-integrated precipitable water, in kg m^{-2}; (e,f) total precipitation, in mm day^{-1}; (g,h) percentage of precipitation that is liquid; and (i,j) annual maximum daily precipitation (Rx1day) in mm day^{-1}. The left column shows the ensemble mean difference (average of HiVarBB ensemble members minus average of SmoothBB ensemble members), with stippling signifying 95% confidence (see Text S1). The right column shows the annual mean value, averaged from 40-90°N, in HiVarBB (black line) and SmoothBB (red line) ensemble members; thick lines denote the ensemble mean, shading denotes the range of each ensemble member set, and vertical gray dashed lines delineate the GFED period (1997–2014).

relative to the SmoothBB simulations (Figure 2d), a difference that is statistically significant (Figure S1b).

Consistent with greater evaporation and atmospheric precipitable water, the HiVarBB emissions also increase precipitation over most regions poleward of 40°N relative to the SmoothBB emissions (Figure 2e). When averaged poleward of 40°N, greater precipitation in the HiVarBB simulations is clear (Figure 2f) and statistically significant (Figure S1c). Specifically, total precipitation poleward of 40°N is 0.5% (0.01 mm/day) greater in the HiVarBB simulations relative to the SmoothBB simulations during the GFED period. There is also a discernible northward shift in the Inter-Tropical Convergence Zone (ITCZ) in the HiVarBB simulations relative to the SmoothBB simulations. This is apparent in Figure 2e as a statistically significant northward ITCZ shift over the Atlantic Ocean and drying of the South Pacific Convergence Zone (SPCZ).

Higher surface temperatures in the NH in the HiVarBB simulations relative to SmoothBB simulations also leads to a shift in precipitation phase. In the NH high latitudes, a larger proportion of precipitation falls as rain rather than snow in HiVarBB ensemble members relative to SmoothBB ensemble members (Figure 2g). Regional differences in the relative amount of liquid precipitation (proportion of liquid to total precipitation) are statistically significant over much of the NH high latitudes. Averaged poleward of 40°N over the GFED period, the proportion of precipitation that falls as rain is 0.8% larger in the HiVarBB ensemble members relative to the SmoothBB ensemble members (Figure 2h) and is statistically significant (Figure S1d). This difference in precipitation phase is most apparent during boreal summer (JJA; Figure S2).

We also find the annual maximum daily precipitation is larger in the HiVarBB simulations compared to SmoothBB simulations over the GFED period for most regions poleward of 40°N. Unlike total precipitation, there is no statistical significance in regional differences in annual maximum daily precipitation (Figure 2i). However, there is statistical significance in the 40-90°N mean difference during the GFED period. Specifically, the annual maximum daily precipitation is 0.7% (0.2 mm/day) larger in the HiVarBB simulations relative to SmoothBB simulations (Figure 2j), and this difference is statistically significant (Figure S1e). Greater intensity of extreme precipitation events in HiVarBB ensemble members compared to SmoothBB ensemble members is generally consistent with greater precipitable water (Allen & Ingram, 2002; Trenberth et al., 2003) and more surface warming (Utsumi et al., 2011).

5 Moderating Factors to Hydrologic Cycle Amplification

As we have shown, the hydrologic cycle is clearly sensitive to the variability in biomass burning emissions. However, compensating atmospheric and ocean processes moderate the extent to which increased biomass burning emissions variability amplifies the hydrologic cycle. Most notably, changes in static stability and relative humidity (RH) act to reduce precipitation efficiency in the HiVarBB simulations. At the same time, larger ocean heat storage and weaker meridional energy convergence act to constrain evaporation increases poleward of 40°N.

Despite greater total precipitation in the HiVarBB simulations, the precipitation efficiency (defined here as the ratio of precipitation to column-integrated precipitable water evaluated locally) is lower in HiVarBB simulations relative to SmoothBB simulations (Figure 3a). The average precipitation efficiency poleward of 40°N is 0.9% (1.7×10^{-8} s^{-1}) lower in HiVarBB ensemble members compared to SmoothBB ensemble members, a difference that is statistically significant (Figure S3a).

Two mechanisms act to lower precipitation efficiency in the the HiVarBB simulations relative to the SmoothBB simulations. First, greater atmospheric black carbon aerosol burdens and atmospheric water vapor in the HiVarBB simulations act together to increase atmospheric absorption of shortwave radiation (Figures S4a, b, c), increasing static stability in the lower troposphere (by increasing moist potential temperature between 990 and 950 hPa; see Figure 3b). Greater static stability in HiVarBB simulations acts to suppress vertical motion and cloud formation relative to the SmoothBB simulations (consistent with O'Gorman & Schneider, 2009; Richter & Xie, 2008). Second, lower RH in the lower troposphere poleward of 40°N in the HiVarBB simulations (Figure 3c), in conjunction with greater specific humidity (Figure S4b), indicates that the difference in atmospheric water vapor capacity is larger than the difference in atmospheric water vapor itself. This deficit is likely caused by water limitations over land, where the largest differences in surface shortwave absorption occur (Figure 1c). Due to lower RH in the HiVarBB simulations, more energy is required to raise air parcels to their lifting condensation level relative to the SmoothBB simulations. Additionally, air parcels are less likely to be lifted to levels where they can

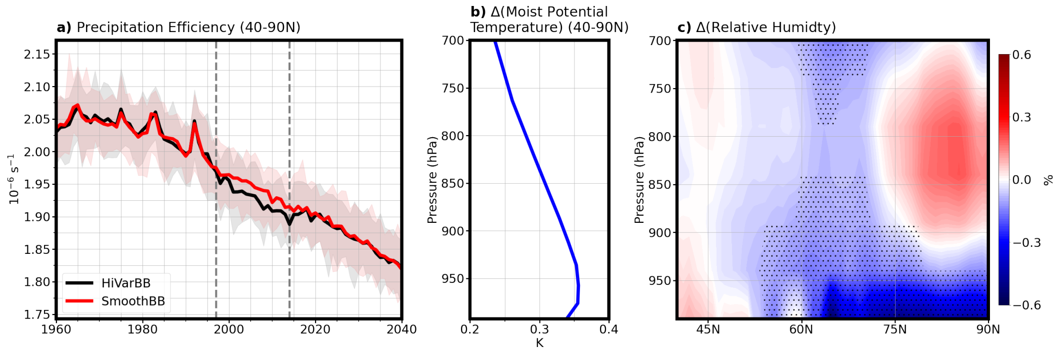

Figure 3. Precipitation efficiency and factors that impact it. (a) total precipitation efficiency, in 10^{-6} s^{-1}, in HiVarBB (black line) and SmoothBB (red line) simulations, with the vertical gray dashed lines delineating the GFED period (1997–2014); (b) ensemble mean difference in the mean 40-90°N vertical moist potential temperature profile, in K; and (c) ensemble mean difference in zonal mean relative humidity from 40-90°N, in %. In (a), thick lines denote the ensemble mean, while the shaded regions denote the range of each ensemble member set. In (b) and (c), the ensemble mean differences are computed as the average of HiVarBB ensemble members minus the average of SmoothBB ensemble members during the GFED period (1997–2014). In (b), the solid line signifies 95% confidence in the significance of the difference between ensemble member sets (see Text S1). In (c), stippling signifies 95% confidence in the significance of the difference between ensemble member sets (see Text S1).

saturate, as the atmosphere is more statically stable in the HiVarBB simulations (Wallace & Hobbs, 2006).

Greater ocean heat storage in HiVarBB simulations also moderates hydrologic cycle amplification, relative to SmoothBB simulations (Figure 4a). Poleward of 40°N, upper ocean heat content (from 0 to 100m depth) is 1.6 ZJ larger in the HiVarBB simulations compared to the SmoothBB simulations during the GFED period, a difference which is statistically significant (Figure S3b). Greater ocean heat storage indicates that not all surplus energy input (from greater surface shortwave radiative fluxes, as shown in Figure 1c) immediately goes to increasing evaporative fluxes, thereby moderating their rise. Greater upper ocean heat content in HiVarBB simulations persists for approximately ten years after the end of the GFED period, indicating that ocean heat storage both moderates and lengthens the time scale of the climate response (as described by Barsugli & Battisti, 1998).

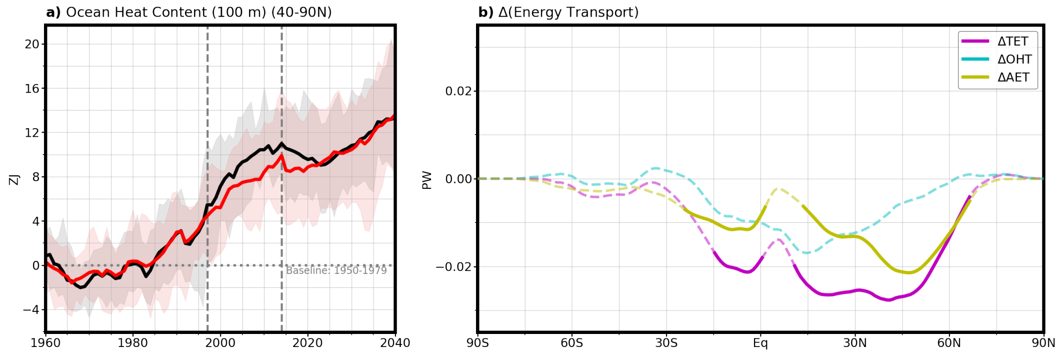

Figure 4. Energetic limitations on hydrologic cycle amplification. (a) upper (top 100 m) ocean heat content anomalies relative to the 1950–1979 average from 40-90°N in HiVarBB (black line) and SmoothBB (red line) simulations, in ZJ; and (b) ensemble mean difference (average of HiVarBB ensemble members minus average of SmoothBB ensemble members) in the meridional northward energy transport during the GFED period (1997–2014), in PW, including total (ΔTET; black line), atmospheric (ΔAET; yellow line), and ocean (ΔOHT; cyan line) components. In (a), thick lines denote the ensemble mean, while shading denotes the range of each member set. In (b), solid lines signify 95% confidence in the significance of the difference between HiVarBB and SmoothBB ensemble member sets (see Text S1).

Adjustments in meridional energy transport further mitigate hydrologic cycle differences poleward of 40°N between HiVarBB and SmoothBB simulations. Figure 4b shows the difference in energy transport between the two simulation ensemble sets, including total, atmospheric, and ocean components. NH total energy transport is lower in HiVarBB simulations relative to SmoothBB simulations (Figure 4b, black line) during the GFED period. This lower energy transport is a response to greater energy input poleward of 40°N (Figure 1c), which tends to flatten the meridional moist static energy gradient and thereby weaken energy transport (Hwang & Frierson, 2010). Indeed, the total atmospheric energy transport is weaker in HiVarBB simulations compared to SmoothBB simulations (Figure 4b, yellow line). This anomalously southward atmospheric energy transport is consistent with a stronger Southern Hemisphere Hadley Cell in HiVarBB simulations (see dry and moist components of atmospheric energy transport in Figure S5) which drives the ITCZ further north (recall Figure 2e) and increases net southward atmospheric energy transport in the tropics (see Kang et al., 2008). Likewise, lower ocean heat transport also contributes to weaker NH total energy transport (Figure 4b, cyan line). Although the lower ocean heat transport is not statistically significant, the weakening of the Atlantic Meridional Ocean Circulation (AMOC) is significant (Figure S6), indicating a decline in ocean heat transport in the Atlantic basin. Weaker meridional energy transport in HiVarBB simulations reduces the energy available for surface warming and evaporation, thereby moderating hydrologic cycle amplification.

6 Implications

Our results provide clear evidence that variability in biomass burning emissions affect the hydrologic cycle. We show that greater biomass burning emissions variability, as used in CMIP6 historical simulations during the GFED period (1997–2014), amplifies the hydrologic cycle in CESM2. Evaporation, atmospheric precipitable water, mean precipitation, precipitation extremes, and fraction of rain precipitation all increase with greater biomass burning emissions variability. This amplification is consistent with the thermodynamic impact of warming (e.g., Allen & Ingram, 2002; Held & Soden, 2006; Stott et al., 2010). Conversely, this hydrologic cycle amplification is moderated by several competing factors: greater static stability and lower RH in HiVarBB ensemble members leads to lower precipitation efficiency; greater ocean heat storage poleward of 40°N moderates the available energy for evaporation over ocean; and weaker meridional energy transport decreases the energy available for surface warming.

It is possible these findings extend to other models participating in CMIP6, not just CESM2. All CMIP6 historical simulations use the same biomass burning emissions, including the increase in variability during the GFED period. Indeed, Fasullo et al. (2021) and DeRepentigny et al. (2021) find evidence of characteristic increases in downwelling shortwave radiation and Arctic sea ice loss, respectively, during the GFED period in several other CMIP6 models. This suggests that other models may also be sensitive to greater biomass burning emissions variability. Further care is required for future treatments of biomass burning emissions variability in historical simulations. If the biomass burning emissions variability over the entire historical and future projection periods was corrected to be more continuous (whether to align with the variability of the GFED estimates, or the estimates prior), the hydrologic cycle would likely change. We note, however, that although each model is subject to the same increase in variability, this does not mean that every model is sensitive to this change (DeRepentigny et al., 2021; Fasullo et al., 2021). We also note that differing model sensitivities to this variability may increase the inter-model spread, and therefore uncertainty, over the GFED period. This highlights the need for further study into how greater biomass burning variability during the GFED period affects hydrologic cycle in a range of CMIP6 models.

As indicated by these findings, care is required when analyzing hydrologic cycle fields within CMIP6 and CESM2-LE historical simulations. Precipitation robustly increases in most areas poleward of 40°N in CMIP6 future projections (Cook et al., 2020). If a baseline includes the GFED period (1997–2014), precipitation increases over future time periods are likely to be computed as lower than if adjacent baseline periods are used. For example, the change in mean precipitation poleward of 40°N from 1995–2015 to 2080–2100 is approximately 7% smaller in the HiVarBB simulations than the SmoothBB simulations. Similar issues are likely even worse for other hydrologic cycle variables, such as atmospheric water vapor, as the relative difference between HiVarBB and SmoothBB simulations is even larger.

Our findings demonstrate that the interannual variability of biomass burning emissions is an important factor that determines the strength of the atmospheric hydrologic cycle. More research is required to better understand the mechanisms driving the climate response to biomass burning emissions variability, particularly that of aerosols and aerosol-adjacent compounds. We underscore the need for studies using multiple models to better parse out the underlying mechanisms by which biomass burning emissions variability impacts the hydrologic cycle and the greater climate system.

Acknowledgments

K.B.H. is supported by the Natural Sciences and Engineering Council of Canada (NSERC), the Province of British Columbia, and the University of Victoria. H.A.S. is supported by base research support through the University of Victoria. P.J.R. is supported by the Pacific Northwest National Laboratory (PNNL) which is operated for DOE by Battelle Memorial Institute under contract DE-AC05-76RL01830. P.D. is supported by the Advanced Study Program of the National Center for Atmospheric Research (NCAR), which is a major facility sponsored by the National Science Foundation (NSF) under Cooperative Agreement No. 1852977. All authors would like to acknowledge the CESM2 Large Ensemble Community Project and supercomputing resources provided by the IBS Center for Climate Physics in South Korea. The CESM project is supported primarily by the NSF. This material is based upon work supported by the National Center for Atmospheric Research (NCAR), which is a major facility sponsored by the NSF under Cooperative Agreement No.

1852977. CESM2-LE data are available here: `https://www.cesm.ucar.edu/projects/community-projects/LENS2/`. Information on the release of the CESM2-LE is available here: `https://doi.org/10.5194/esd-2021-50`.

References

Allen, M. R., & Ingram, W. J. (2002). Constraints on future changes in climate and the hydrologic cycle. *Nature*, *419*(6903), 228–232. doi: 10.1038/nature01092

Barsugli, J. J., & Battisti, D. S. (1998). The basic effects of atmosphere–ocean thermal coupling on midlatitude variability. *Journal of the Atmospheric Sciences*, *55*(4), 477–493. doi: 10.1175/1520-0469(1998)055⟨0477:TBEOAO⟩2.0.CO;2

Boucher, O., Randall, D., Artaxo, P., Bretherton, C., Feingold, G., Forster, P., ... Zhang, X. (2013). Chapter 7: Clouds and Aerosols. *Climate Change 2013: The Physical Science Basis. Contribution of Working Group I to the Fifth Assessment Report of the Intergovernmental Panel on Climate Change*, 571–658. doi: 10.1017/CBO9781107415324.016

Cook, B. I., Mankin, J. S., Marvel, K., Williams, A. P., Smerdon, J. E., & Anchukaitis, K. J. (2020). Twenty-first century drought projections in the CMIP6 forcing scenarios. *Earth's Future*, *8*(6). doi: 10.1029/2019EF001461

Danabasoglu, G., Lamarque, J. F., Bacmeister, J., Bailey, D. A., DuVivier, A. K., Edwards, J., ... Strand, W. G. (2020). The Community Earth System Model Version 2 (CESM2). *Journal of Advances in Modeling Earth Systems*, *12*(2). doi: 10.1029/2019MS001916

DeRepentigny, P., Jahn, A., Holland, M. M., Fasullo, J., Lamarque, J.-F. O., Hannay, C., ... Barrett, A. (2021). Enhanced early 21st century Arctic sea ice loss due to CMIP6 biomass burning emissions. *Nature Climate Change*. (Submitted)

Fasullo, J. T., Lamarque, J.-F., Hannay, C., Rosenblum, N., DeRepentigny, P., Jahn, A., & Deser, C. (2021). Spurious late historical-era warming in CESM2 and other CMIP6 climate simulations driven by prescribed biomass burning emissions. *Geophysical Research Letters*. (Submitted)

Flato, G., Marotzke, J., Abiodun, B., Braconnot, P., Chou, S., Collins, W., ... Rummukainen, M. (2013). Chapter 9: Evaluation of Climate Models. *Climate Change 2013: The Physical Science Basis. Contribution of Working Group I to the Fifth Assessment Report of the Intergovernmental Panel on Climate Change*, 741–866. doi:

10.1017/CBO9781107415324.020

Held, I. M., & Soden, B. J. (2006). Robust responses of the hydrological cycle to global warming. *Journal of Climate*, *19*, 5686–1560. doi: 10.1175/2010JCLI4045.1

Hoesly, R. M., Smith, S. J., Feng, L., Klimont, Z., Janssens-Maenhout, G., Pitkanen, T., ... Zhang, Q. (2018). Historical (1750–2014) anthropogenic emissions of reactive gases and aerosols from the Community Emissions Data System (CEDS). *Geoscientific Model Development*, *11*(1), 369–408. doi: 10.5194/gmd-11-369-2018

Hunke, E. C., Lipscomb, W. H., Turner, A. K., Jeffery, N., & Elliot, S. (2015). *CICE: The Los Alamos Sea Ice Model Documentation and Software User's Manual Version 5.1* (Tech. Rep. No. LA-CC-06-012). Los Alamos National Laboratory.

Hwang, Y.-T., & Frierson, D. M. W. (2010, 12). Increasing atmospheric poleward energy transport with global warming. *Geophysical Research Letters*, *37*(24). doi: 10.1029/2010GL045440

Jungclaus, J. H., Bard, E., Baroni, M., Braconnot, P., Cao, J., Chini, L. P., ... Zorita, E. (2017). The PMIP4 contribution to CMIP6 - Part 3: The last millennium, scientific objective, and experimental design for the PMIP4 past1000 simulations. *Geoscientific Model Development*, *10*(11), 4005–4033. doi: 10.5194/gmd-10-4005-2017

Kang, S. M., Held, I. M., Frierson, D. M. W., & Zhao, M. (2008). The response of the ITCZ to extratropical thermal forcing: Idealized slab-ocean experiments with a GCM. *Journal of Climate*, *21*(14), 3521–3532. doi: 10.1175/2007JCLI2146.1

Kiehl, J. T. (2007). Twentieth century climate model response and climate sensitivity. *Geophysical Research Letters*, *34*(22). doi: 10.1029/2007GL031383

Kravitz, B., Robock, A., Tilmes, S., Boucher, O., English, J. M., Irvine, P. J., ... Watanabe, S. (2015). The Geoengineering Model Intercomparison Project phase 6 (GeoMIP6): Simulation design and preliminary results. *Geoscientific Model Development*, *8*(10), 3379–3392. doi: 10.5194/gmd-8-3379-2015

Lamarque, J. F., Bond, T. C., Eyring, V., Granier, C., Heil, A., Klimont, Z., ... Vuuren, D. P. V. (2010). Historical (1850-2000) gridded anthropogenic and biomass burning emissions of reactive gases and aerosols: Methodology and application. *Atmospheric Chemistry and Physics*, *10*(15), 7017–7039. doi: 10.5194/acp-10-7017-2010

Lawrence, D. M., Fisher, R. A., Koven, C. D., Oleson, K. W., Swenson, S. C., Bonan, G., ... Zeng, X. (2019). The community land model version 5: Description of new features, benchmarking, and impact of forcing uncertainty. *Journal of Advances in Modeling*

Earth Systems, *11*(12), 4245–4287. doi: 10.1029/2018MS001583

Liu, X., Ma, P. L., Wang, H., Tilmes, S., Singh, B., Easter, R. C., ... Rasch, P. J. (2016). Description and evaluation of a new four-mode version of the Modal Aerosol Module (MAM4) within version 5.3 of the Community Atmosphere Model. *Geoscientific Model Development*, *9*(2), 505–522. doi: 10.5194/gmd-9-505-2016

O'Gorman, P. A., & Schneider, T. (2009). The physical basis for increases in precipitation extremes in simulations of 21st-century climate change. *Proceedings of the National Academy of Sciences*, *106*(35), 14773–14777. doi: 10.1073/pnas.0907610106

O'Neill, B. C., Tebaldi, C., Vuuren, D. P. V., Eyring, V., Friedlingstein, P., Hurtt, G., ... Sanderson, B. M. (2016). The Scenario Model Intercomparison Project (ScenarioMIP) for CMIP6. *Geoscientific Model Development*, *9*(9), 3461–3482. doi: 10.5194/gmd-9-3461-2016

Pandis, S. N., Harley, R. A., Cass, G. R., & Seinfeld, J. H. (1992). Secondary organic aerosol formation and transport. *Atmospheric Environment. Part A. General Topics*, *26*(13), 2269–2282. doi: 10.1016/0960-1686(92)90358-R

Ramanathan, V., Crutzen, P. J., Kiehl, J. T., & Rosenfeld, D. (2001). Aerosols, climate, and the hydrological cycle. *Science*, *294*(5549), 2119–2124. doi: 10.1126/science.1064034

Richter, I., & Xie, S. P. (2008). Muted precipitation increase in global warming simulations: A surface evaporation perspective. *Journal of Geophysical Research Atmospheres*, *113*(24). doi: 10.1029/2008JD010561

Rodgers, K. B., Lee, S.-S., Rosenbloom, N., Timmermann, A., Danabasoglu, G., Deser, C., ... Yeager, S. G. (2021). Ubiquity of human-induced changes in climate variability. *Earth System Dynamics*. doi: 10.5194/esd-2021-50

Seinfeld, J. H., Bretherton, C., Carslaw, K. S., Coe, H., Demott, P. J., Dunlea, E. J., ... Wood, R. (2016). Improving our fundamental understanding of the role of aerosol cloud interactions in the climate system. *Proceedings of the National Academy of Sciences*, *113*(21), 5781–5790. doi: 10.1073/pnas.1514043113

Smith, R., Jones, P., Briegleb, B., Bryan, F., Danabasoglu, G., Dennis, J., ... Yeager, S. (2010). The Parallel Ocean Program (POP) reference, manual ocean component of the Community Climate System Model (CCSM) and Community Earth System Model (CESM). *LANL Tech. Report*.

Stott, P. A., Gillett, N. P., Hegerl, G. C., Karoly, D. J., Stone, D. A., Zhang, X., & Zwiers, F. (2010). Detection and attribution of climate change: A regional perspective. *Wiley*

Interdisciplinary Reviews: Climate Change, *1*(2), 192–211. doi: 10.1002/wcc.34

Trenberth, K. E., Dai, A., Rasmussen, R. M., & Parsons, D. B. (2003). The changing character of precipitation. *Bulletin of the American Meteorological Society*, *84*(9), 1205–1218. doi: 10.1175/BAMS-84-9-1205

Utsumi, N., Seto, S., Kanae, S., Maeda, E. E., & Oki, T. (2011). Does higher surface temperature intensify extreme precipitation? *Geophysical Research Letters*, *38*(16). doi: 10.1029/2011GL048426

van der Werf, G. R., Randerson, J. T., Giglio, L., Leeuwen, T. T. V., Chen, Y., Rogers, B. M., … Kasibhatla, P. S. (2017). Global fire emissions estimates during 1997-2016. *Earth System Science Data*, *9*(2), 697–720. doi: 10.5194/essd-9-697-2017

van Marle, M. J., Kloster, S., Magi, B. I., Marlon, J. R., Daniau, A. L., Field, R. D., … Werf, G. R. V. D. (2017). Historic global biomass burning emissions for CMIP6 (BB4CMIP) based on merging satellite observations with proxies and fire models (1750-2015). *Geoscientific Model Development*, *10*(9), 3329–3357. doi: 10.5194/gmd-10-3329-2017

Wallace, J. M., & Hobbs, P. V. (2006). *Atmospheric science: An introductory survey* (Second ed.). Academic Press. doi: 10.1016/C2009-0-00034-8

Wilks, D. S. (2016). "The stippling shows statistically significant grid points": How research results are routinely overstated and overinterpreted, and what to do about it. *Bulletin of the American Meteorological Society*, *97*(12), 2263–2273. doi: 10.1175/BAMS-D-15-00267.1

Zanchettin, D., Khodri, M., Timmreck, C., Toohey, M., Schmidt, A., Gerber, E. P., … Tummon, F. (2016). The Model Intercomparison Project on the climatic response to Volcanic forcing (VolMIP): Experimental design and forcing input data for CMIP6. *Geoscientific Model Development*, *9*(8), 2701–2719. doi: 10.5194/gmd-9-2701-2016

Supporting Information for "Increased Variability of Biomass Burning Emissions in CMIP6 Amplifies Hydrologic Cycle in the CESM2 Large Ensemble"

Kyle B. Heyblom[1], Hansi A. Singh[1], Philip J. Rasch[2,3], Patricia DeRepentigny[4]

[1]University of Victoria, School of Earth and Ocean Sciences, Victoria, BC, Canada

[2]Pacific Northwest National Laboratory, Atmospheric Sciences and Global Change Division, U.S. DOE Office of Science, Richland, WA, USA

[3]University of Washington, Department of Atmospheric Science, Seattle, WA, USA

[4]National Center for Atmospheric Research, Climate and Global Dynamics Laboratory, Boulder, CO, USA

Contents of this file

1. Text S1
2. Figures S1 to S7

Introduction

Here, we present the methods we used to evaluate statistical significance (Text S1-S2), as well as supplemental figures that further our findings on differences between CMIP6 (HiVarBB) and smoothed (SmoothBB) biomass burning emission scenarios in the CESM2 Large Ensemble. These figures show: statistical significance of area-averaged differences of metrics shown in Figure 2 (Figure S1), seasonal differences in relative liquid precipitation (Figure S2), statistical significance of differences in precipitation efficiency and ocean heat content (Figure S3), differences in atmospheric and cloud properties (Figure S4), differences in the moist and dry atmospheric energy transport components (Figure S5), and differences in the Atlantic meridional overturning circulation (AMOC; Figure S6).

Text S1. Evaluating spatial statistical significance. We assess spatial (i.e., grid point, zonally-averaged, and vertical profile) statistical significance using a Welch's t-test. We additionally limit significance determinations for false discoveries using the recommendations made by Wilks (2016). We use an α_{FDR} of 0.10 to approximate a global significance level of 0.05.

Text S2. Evaluating area-averaged statistical significance. We use a non-parametric bootstrapping approach to determine the statistical significance of the area-average differences between fields in HiVarBB and SmoothBB ensemble member sets. We conduct this test by randomly dividing all 80 members into two groups and determining the difference in the means of each group. We repeat this random selection a hundred thousand times to develop a distribution of random differences. We determine significance if the mean difference between the HiVarBB and SmoothBB ensemble member sets is outside of the 2.5 and 97.5 percentile range, signifying the two-tail 95% confidence interval of the distribution of differences between randomly divided members. This test allows us to determine whether, with 95% confidence, the mean difference between the HiVarBB and

SmoothBB ensemble member sets is greater than what could be generated by chance if the mean difference was only influenced by internal variability. To verify that significant differences are unique to the GFED period, we also conduct sensitivity tests by running the test over multiple time periods, both before and after the GFED period.

References

Wilks, D. S. (2016). "The stippling shows statistically significant grid points": How research results are routinely overstated and overinterpreted, and what to do about it. *Bulletin of the American Meteorological Society*, *97*(12), 2263–2273. doi: 10.1175/BAMS-D-15-00267.1

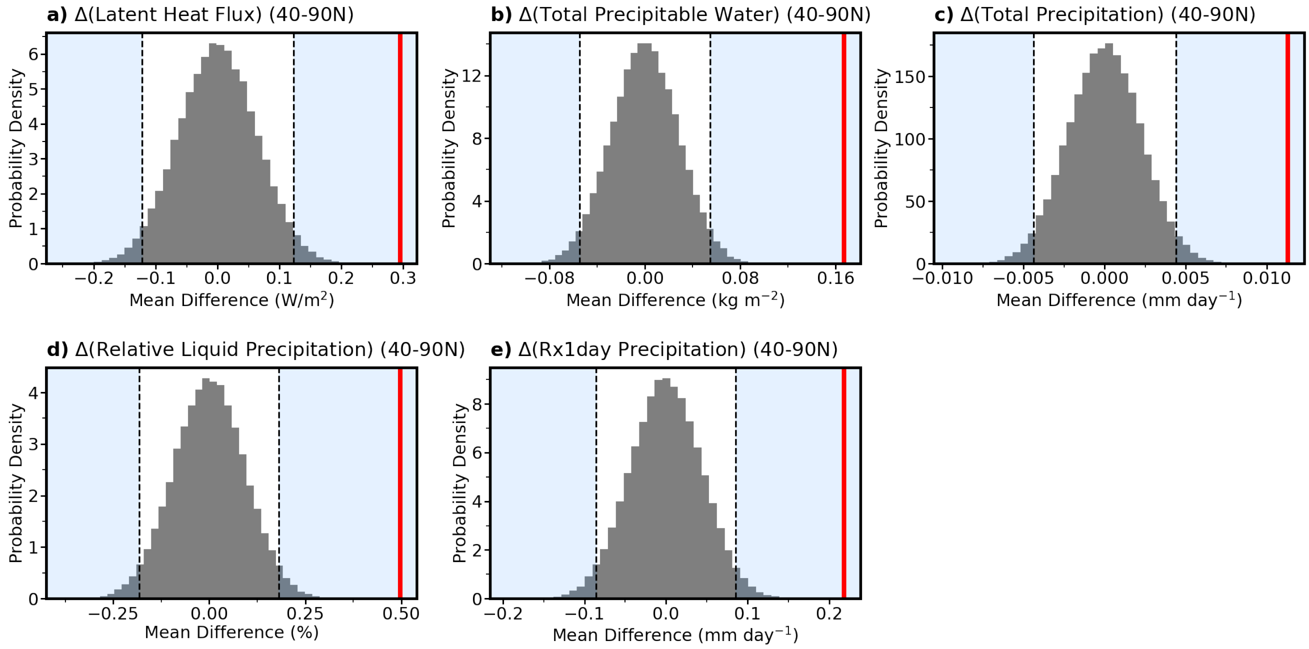

Figure S1. Statistical significance of area-averaged differences in the atmospheric hydrologic cycle. (a) latent heat flux, in W m^{-2}; (b) column-integrated precipitable water, in kg m^{-2}; (c) total precipitation, in mm day^{-1}; (d) percentage of precipitation that is liquid; and (e) annual maximum daily precipitation (Rx1day) in mm day^{-1}, all from 40-90°N over the GFED period (1997–2014). The gray histogram shows a probability density distribution of means derived from a non-parametric bootstrapping test (see Text S2), and the blue shading indicates the region outside of the (two-sided) 95% confidence intervals; the difference between HiVarBB and SmoothBB ensemble means (red line) is statistically significant (at the 95% level) if it falls within the blue shaded region.

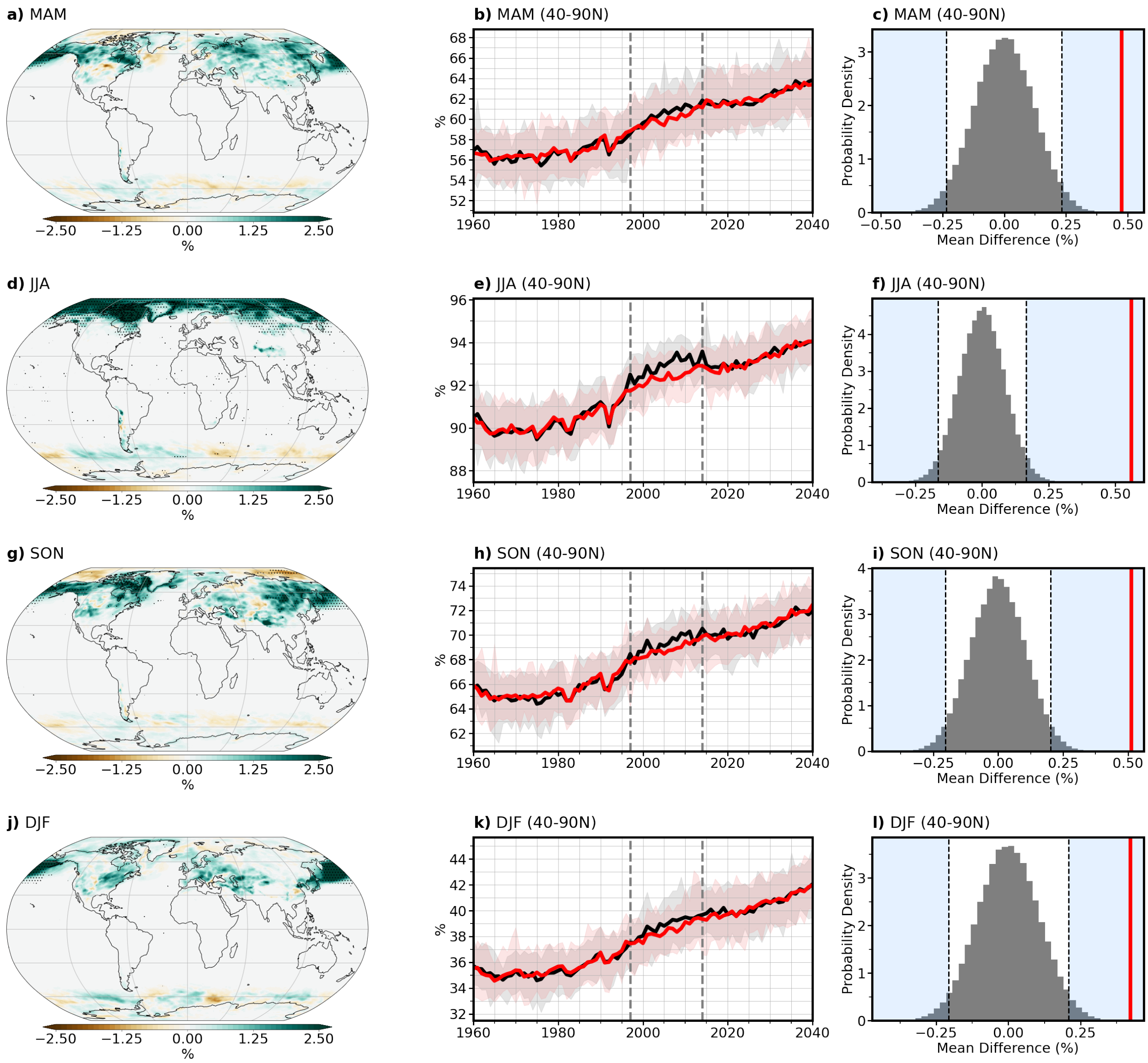

Figure S2. Differences in seasonal relative liquid precipitation. The left and middle columns are the same as in Figure 2, but showing differences in percentage of precipitation that is liquid in (a-c) March-May (MAM), (d-f) June-August (JJA), (g-i) September-November (SON), (j-l) and December-February (DJF). The right column shows the statistical significance of the difference in HiVarBB and SmoothBB ensemble means from 40-90°N over the GFED period. The gray histogram shows a probability density distribution of means derived from a non-parametric bootstrapping test (see Text S2), and the blue shading indicates the region outside of the (two-sided) 95% confidence intervals. The difference between HiVarBB and SmoothBB ensemble means (red line) is statistically significant (at the 95% level) if it falls within the blue shaded region.

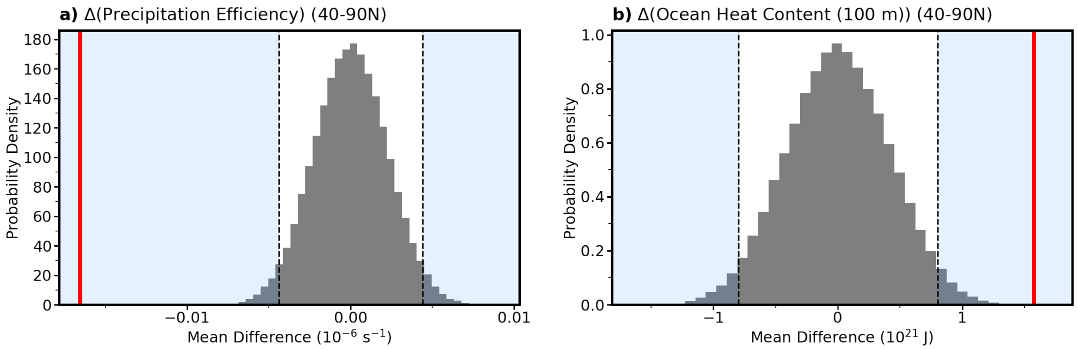

Figure S3. Statistical significance of area-averaged differences in moderating factors. (a) precipitation efficiency, and (b) upper (top 100 m) ocean heat content from 40-90°N during the GFED period (1997–2014). The gray histogram shows a probability density distribution of means derived from a non-parametric bootstrapping test (see Text S2), and the blue shading indicates the region outside of the (two-sided) 95% confidence intervals. The difference between HiVarBB and SmoothBB ensemble means (red line) is statistically significant (at the 95% level) if it falls within the blue shaded region.

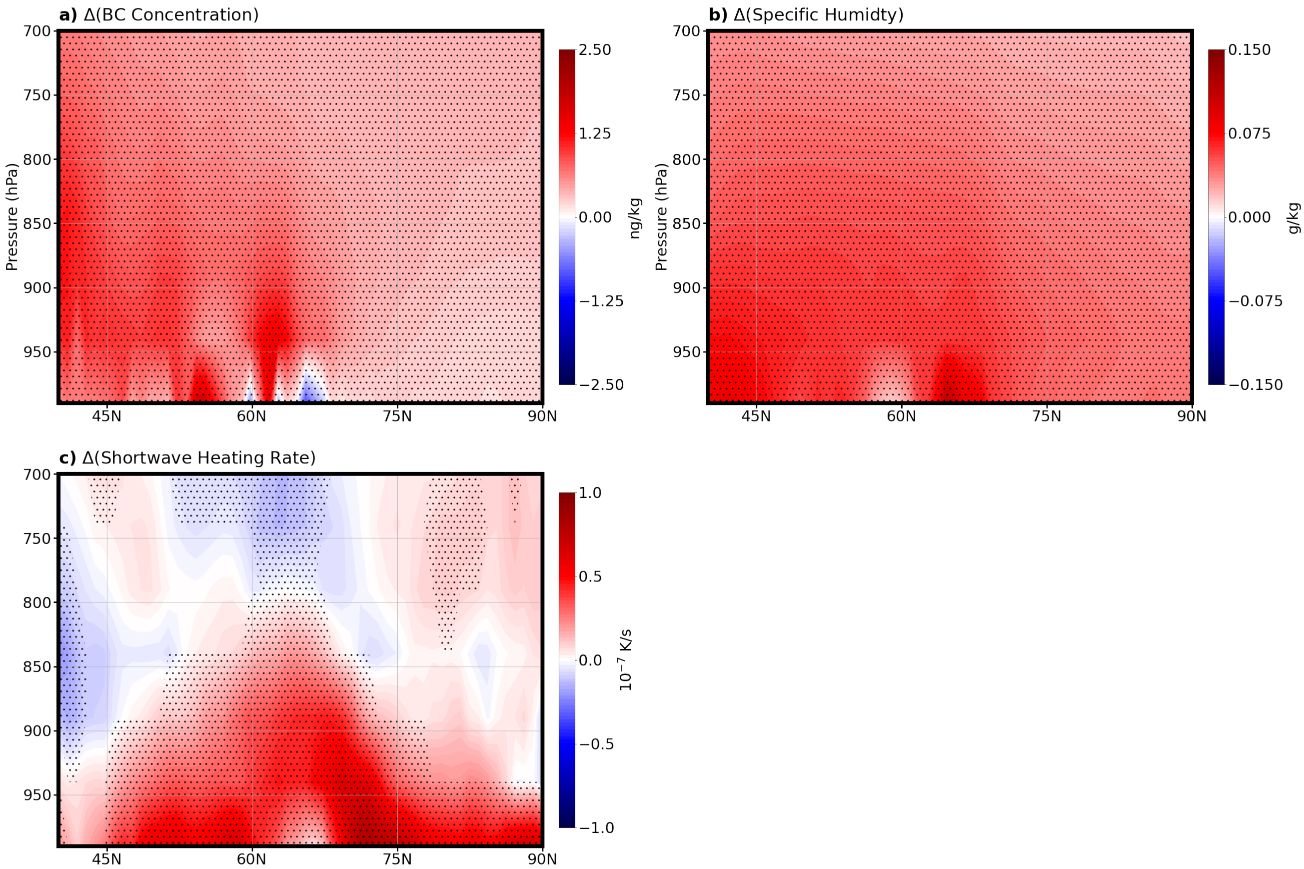

Figure S4. Zonal-mean ensemble mean difference of mechanisms affecting the precipitation efficiency. (a) black carbon concentration (in ng/kg), (b) specific humidity (in g/kg), (c) shortwave heating rate (in 10^{-7} K/s) from 40-90°N. Ensemble mean differences are computed as as the average of HiVarBB ensemble members minus the average of SmoothBB ensemble members during the GFED period (1997–2014). Stippling signifies 95% confidence in the significance of the difference between ensemble member sets (see Text S1).

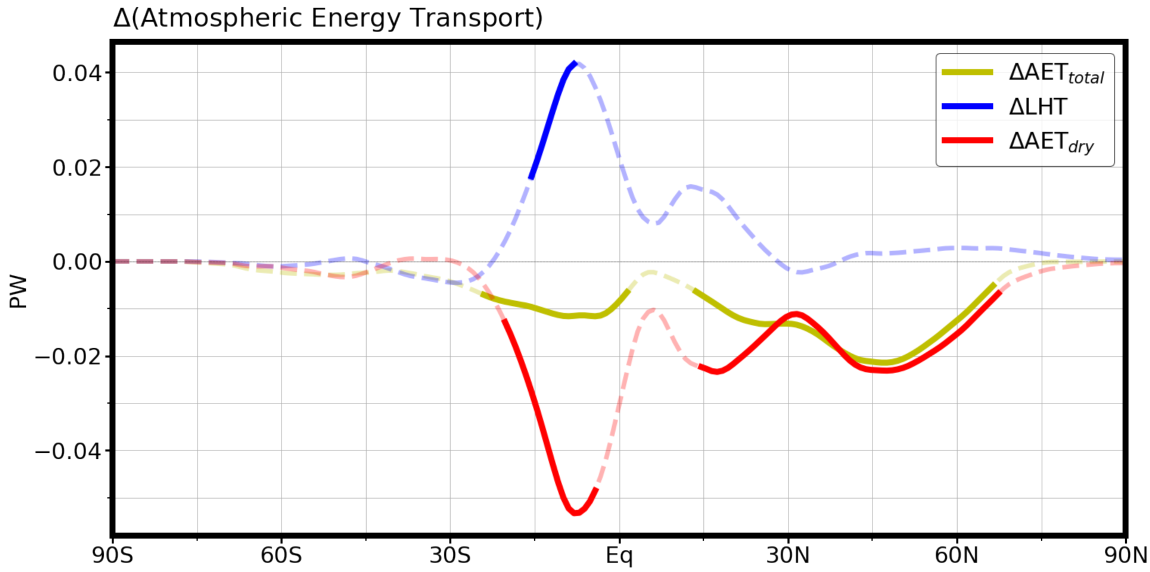

Figure S5. Differences in meridional atmospheric energy transport components. Ensemble mean difference (average of HiVarBB ensemble members minus average of SmoothBB ensemble members) in the total atmospheric energy transport (ΔAET_{total}, yellow line), latent heat transport (ΔLHT, blue line), and dry static energy transport (ΔAET_{dry}, red line) during the GFED period (1997–2014), in PW. Solid lines signify 95% confidence in the significance of the difference between HiVarBB and SmoothBB ensemble member sets (see Text S1).

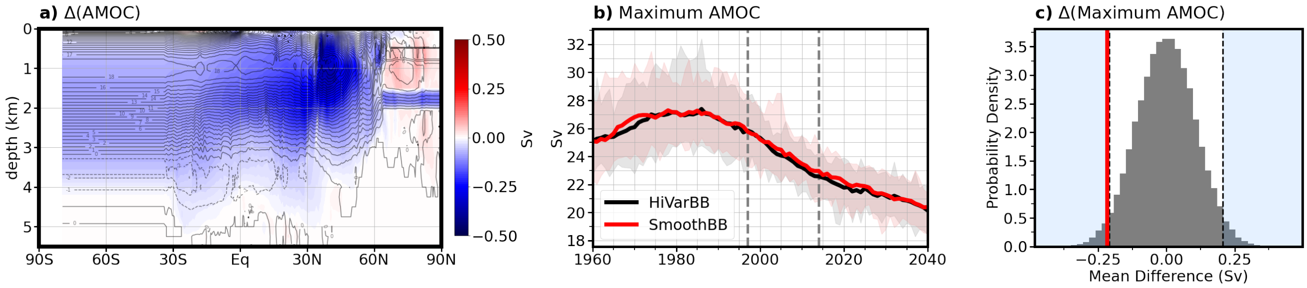

Figure S6. Differences in Atlantic meridional overturning circulation (AMOC). (a) zonal-mean ensemble mean difference (average of HiVarBB ensemble members minus average of the SmoothBB ensemble members), (b) annual mean Atlantic meridional overturning maximum from HiVarBB (black curve) and SmoothBB (red curve) ensemble members; thick lines denote the ensemble mean, shading denotes one standard deviation of each ensemble member set, and horizontal gray dotted lines delineate the GFED period (1997–2014), and (c) statistical significance of the difference in Atlantic meridional overturning maximum ensemble means during the GFED period. The gray histogram shows a probability density distribution of means derived from a non-parametric bootstrapping test (see Text S2), and the blue shading indicates the region outside of the (two-sided) 95% confidence intervals. The difference between HiVarBB and SmoothBB ensemble means (red line) is statistically significant (at the 95% level) if it falls within the blue shaded region.